

Massively Parallel Computation of Accurate Densities for N-body Dark Matter Simulations using the Phase-Space-Element Method

Ralf Kaehler

*Kavli Institute for Particle Astrophysics and Cosmology,
SLAC National Accelerator Laboratory
Menlo Park, CA 94025, USA*

Abstract

In 2012 a method to analyze N-body dark matter simulations using a tetrahedral tessellation of the three-dimensional dark matter manifold in six-dimensional phase space was introduced.

This paper presents an accurate density computation approach for large N-body datasets, that is based on this technique and designed for massively parallel GPU-clusters. The densities are obtained by intersecting the tessellation with the cells of a spatially adaptive grid structure. We speed up this computational expensive part with an intersection algorithm, that is tailored to modern GPU architectures. We discuss different communication and dynamic load-balancing strategies and compare their weak and strong scaling efficiencies for several large N-body simulations.

Keywords: parallel algorithms, dark matter, n-body simulations, graphics processors

1. Motivation

Dark matter is a key component in state-of-the-art large-scale structure formation theories, and N-body simulations have become an essential method to test their predictions by comparing them to observational data, for example, the large-scale distribution of galaxies and galaxy clusters. This numerical approach treats dark matter as a collisionless gas that is sampled by a set of particles of equal mass, whose positions are updated over time according to the overall gravitational forces at the tracers positions, e. g. *ART* [1], *Ramses* [2], *Gadget2* [3], *HACC* [4], *2HOT* [5], *Enzo* [6] and *NyX* [7].

An integral part of N-body simulations and their analysis codes is the computation of accurate mass densities, e. g., to solve the Poisson equation, identify features of the cosmic web or to predict dark matter annihilation signals. Various techniques, to extrapolate from the mass at the discrete particle positions to a density field defined everywhere in the computational domain, have

been introduced. *Particles Mesh* codes, for example, construct the underlying density field at the vertices, respectively cells of an auxiliary grid structure. The simplest technique, also known as *Nearest Grid Point (NGP)* [8], assigns the mass associated with each particle to the grid cell that contains it. The *Cloud-In-Cell* [9] approach models the particle’s mass distribution as a cube centered at its position and distributes the mass proportionally to all overlapping cells. *Smoothed-Particle Hydrodynamics (SPH)* schemes superimpose rotationally symmetric kernel functions centered at the particle positions [10]. Another technique constructs Voronoi tessellations and estimates the densities from the volumes of the cells enclosing each particle [11]. However, the densities generated by all these methods are subject to artifacts due to sampling noise inherent to the underlying discrete distributions, which is problematic in many application scenarios.

In 2012 a method that allows the computation of densities from N-body simulations, not affected by the above-mentioned Poisson noise, was introduced [12, 13]. The basic idea is to use the particles, to construct a tessellation of the 3-dimensional dark matter sheet, embedded in 6-dimensional phase space and instead of assuming that the mass is concentrated at discrete locations, it is spread out across the elements of the tessellation. Projecting the tessellation into configuration space and adding the density contributions from all elements that overlap the same spatial location, gives rise to well-defined densities in the entire computational domain.

In recent years this method has been successfully applied to tackle problems in various applications that arose from the noise of the previous methods, like reducing artificial clumping in N-body simulations [14], improving the quality of visualizations of dark matter simulations [15, 16], the creation of smooth maps of the gravitational lensing potential around dark matter halos [17], studying the statistics of cosmic velocity fields [18], the construction of new numerical schemes for dark matter simulations [19], and the method has even inspired work in computational geometry [20].

A drawback of the phase-space tessellation approach is its computational complexity for processing the large amounts of resulting tessellation elements. Fortunately the inherently parallel nature of the problem is well-suited for massively parallel, heterogeneous cluster architectures equipped with accelerators, which have become more and more popular in the last decade, due to their energy and cost efficiency.

This paper presents a phase-space tessellation-based density computation approach for large N-body dark matter simulation, data that is tailored to massively parallel (GPU-)cluster environments, enabling the handling of highly complex tessellations. The mass associated with the tetrahedral elements is sampled onto a block-structured grid with locally adaptive resolution, utilizing an exact tetrahedron-cube intersection algorithm tailored to massively parallel GPU architectures. In order to efficiently utilize the available computational resources, the resolution of the deposit grid is locally refined, based on the features of the underlying tessellation. Another crucial ingredient for the overall performance is an efficient load balancing scheme, that distributes the workload

equally across the cluster, while minimizing data transfers and local memory requirements for storing the tessellation elements. We discuss two dynamic schemes - the first exchanges tessellation elements between compute nodes and deposits all tetrahedra, required for each part of the grid structure, locally on a different node of the cluster, whereas the second one processes only elements that are locally available on each node, followed by a global reduction operation to obtain the overall mass per cell. We end the paper with a detailed analysis of the algorithm for various datasets of up to 4096^3 particles, including several weak and strong scaling tests.

2. Review of the Phase-Space Element Approach

In this section, we briefly review the main ideas of the phase-space tessellation method, that are most relevant for this paper. For a detailed discussion please refer to [12, 13]. N-body simulations model the large-scale evolution of dark matter in the Universe using point-like mass sources, called *tracer particles* or just *tracers* in the following, each typically carrying between 10^6 and 10^9 solar masses. The positions of the tracers are updated according to the aggregate gravitational forces under the assumption, that the mass of the physical dark matter particles represented by the tracers, is centered at the tracer positions. However, it is physically more accurate to regard dark matter as a collisionless fluid that is governed by the *Vlasov-Poisson equation* [21], with the tracer particle’s mass being spread out over the computational domain, instead of being concentrated at a set of quite arbitrary discrete sampling locations, as illustrated in the 2-dimensional phase-space diagram in Figure 1.

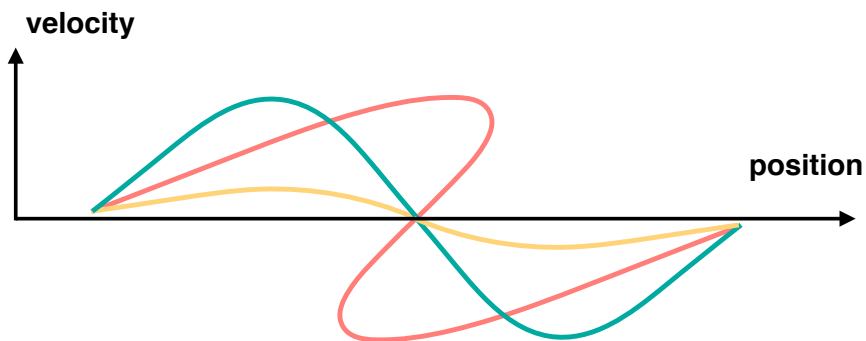


Figure 1: This 2D phase-space diagram shows the positions and velocities of the dark matter fluid for three different time-steps. Initially, the dark matter fluid is almost uniformly distributed and at rest (yellow), but over time, gravity accelerates the dark fluid elements which gain velocity (green). At later times, several streams of the dark matter fluid co-exist at the same spatial regions (red).

At the initial time step, the tracer particles are distributed almost uniformly throughout the computational domain, with their positions aligned with the vertices of a regular grid. We will refer to this arrangement as the *Lagrangian grid* in the following. Given that each cell initially has the same volume and

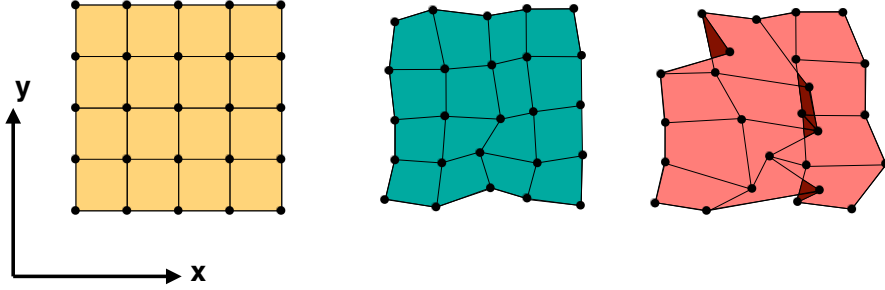


Figure 2: A 2D configuration space illustration of a regular grid structure defined by the tracer particles of an N-body simulation run. Initially, the particles are distributed regularly over the computational domain (left). Over time the particles are advected due to gravitational forces and the corresponding cells become deformed (middle). At later times, cells will start to overlap (dark shaded region on the right).

that the mass is distributed homogeneously across the computational domain, the same mass is assigned to each cell. In this approach the cell connectivity is constant over time, whereas the spatial locations of the vertices are updated according to the actual positions of the tracer particles, causing a deformation of the embedded logical rectangular Lagrangian grid in configuration space, as depicted in Figure 2. Given the constant mass per cell, the knowledge of its time-dependent volume allows the estimation of its local density. However, instead of directly using the deformed cells to compute these volumes, it is computational more efficient to first tessellate them by tetrahedra, as these are always convex, independently of the relative positions of their vertices. We will follow the tessellation choice using 6 tetrahedra as for example used in [15]. So if m is the constant mass per cell and $\sum_i V_i(\mathbf{x}, t)$ the total volume of all tetrahedra that cover the location \mathbf{x} at time t , the total mass density is given by

$$\rho_{tot}(\mathbf{x}, t) = m \sum_i \frac{1}{V_i(\mathbf{x}, t)}. \quad (1)$$

3. Distributed Tessellation Construction

In this Section, we discuss how the tetrahedral tessellation is constructed in a distributed environment, starting with the N-body simulation's data output. Our goal is to assign approximately the same number of elements to each node,

while exploiting as much spatial locality as possible, in order to reuse tracers that are shared between multiple elements.

Our strategy is to subdivide the underlying logical Lagrangian grid, see discussion in Section 2, into rectangular blocks, and assign them to different cluster nodes. Adjacent blocks share a layer of tracer particles on common boundary faces, edges or corners, ensuring that each individual node has access to all data required to locally construct the tetrahedra associated with the cells of its block.

Large-scale N-body simulation codes usually store their data in spatially clustered arrangements, e. g. employ space-filling Hilbert-curves [3] or Morton-order layouts[5]. Hence, the data is already partially organized in blocks in Lagrangian grid space, in particular for the earlier timesteps. And because the tracer particles typically travel relatively small fractions of the overall spatial extent of the computational domain, the correlation between chunks of data on disk and blocks in Lagrangian grid space is partly conserved over time. Exploiting this clustering is crucial in order to reduce the amount of internode communication during the construction of the tetrahedral elements, which implies that the file offset for the chunks of data each compute node reads from disk, should be consistent with its assigned Lagrangian block position.

However, in general, a fraction of the tracers will be unavailable on each node, thus requiring compute nodes to exchange missing data. In order to facilitate this, each node organizes its particles in different bins, one for each target node, which is computed from the particle’s unique ID. Due to the shared boundary layers between adjacent Lagrangian blocks, a particle may have to be sent to up to 8 different nodes und thus is duplicated in several bins. However, while this introduces only a small memory overhead, it avoids expensive search operations and allows to free entire data arrays efficiently when the pairwise communication between certain nodes has been carried out. Once a node received all particle data for its local block, the tracers are sorted by their IDs, which become obsolete and are deleted.

4. Constructing the Adaptive Grid Structure

In this section, we discuss the distributed construction of the adaptive deposit grid structure. We decided to use an Oct-tree for this purpose, although an extension to more general structures like AMR (adaptive mesh refinement) trees would be possible, too.

Starting at the root node, associated with the minimal axis-aligned bounding box containing all tracer particles in the computational domain, each compute node detects the number of local tetrahedra that cover each tree node and obtains the overall number via a global reduction operation. If it is above user-defined threshold, the bounding box is refined by 8 children and the process continues recursively until the number of elements that partially overlap a tree node’s region is below the threshold or a minimal node extension is reached. The latter is necessary because the number of tetrahedra does not always decrease on the refined regions, for example, once it is completely contained inside the

intersection of a set of tetrahedra. The leaf nodes of the tree are overlaid by cubical grid patches of the same number of cells and thus yield a sampling of the computational domain, whose local resolution is adapted to the features of the underlying density of tetrahedra.

A drawback of the approach discussed so far are its high memory requirements. In order to efficiently check the refinement criterion, one has to keep track of sets of local tetrahedra that cover different parts of the tree, e.g. by storing their unique IDs for each node of the tree. However, given that the number of tetrahedra exceeds the number of tracer particles by a factor of about 6, and at least 64-bit integers are necessary to uniquely identify them, even in the optimal case that each element falls into exactly one leaf node and thus needs to be stored only once, the memory requirements would vastly exceed the one required for storing the original tracer positions.

In order to reduce this overhead, each compute node first partitions its local Lagrangian grid block into a set of subregions, called subblocks in the following, and precomputes the partially overlapping, minimal axis-aligned bounding boxes enclosing the particles of each subregion. Instead of testing each tetrahedron individually, the intersections between these precomputed bounding boxes and the domains of the tree nodes used and only the IDs of intersecting subblock are stored for each tree node, thus drastically reducing the memory overhead. The number of tetrahedra that overlap a specific tree node is estimated using the intersection volume between the nodes and the subblocks' bounding boxes, assuming that each tetrahedron in the subblock has a similar volume and the tree node is subdivided, if the estimate exceeds the given threshold. We found that a number 8^3 cells for each subblock works well for our applications.

5. Dynamic Load Balancing

For typical dark matter simulations, the tetrahedra density will vary substantially across the computational domain, ranging from a few elements per point in underdense voids, to several thousand in the regions of dark matter halos. To some extent, we account for this variance by adapting the spatial resolution of the oct-tree to the density of the underlying tessellation. However, even with this approach, the workload usually differs for the leaf nodes of the tree, so an efficient load-balancing technique is crucial for optimally utilizing the computational resources.

We employ adaptive load balancing strategies on three different levels: between individual compute nodes, between individual CPU threads per compute node, as well as on the level of GPU kernel calls, launched by the CPU threads. The latter two will be discussed in detail in Section 6, while here we focus on load balancing the work per compute node.

In general, the tetrahedra required for depositing the mass onto a leaf node of the tree structure will be scattered across multiple compute nodes. We will discuss two approaches for processing each leaf: (A) gathering all required tetrahedra on one compute node, which deposits the elements' masses and stores the

final cubical deposit patch, or (B) alternatively depositing only the local tetrahedra on each compute node, followed by a reduction operation between all processes, that contributed to the same leaf. In the next two paragraphs, we will describe our implementations of these approaches using MPI, while we discuss a comparison between them in terms of performance in Section 7. In both cases, we launch one MPI rank per compute node and at least two CPU threads per MPI rank to overlap the local computation required for depositing the mass with the internode communication.

(A) *Sending Point Data.* Here each MPI rank enters a loop and signals all other ranks if it is ready for new work or not. This is done by setting a flag in a bitmask, with one entry for each rank, that is globally reduced. The first rank R , that is ready for new work, is assigned the entry out of the list of remaining leaves, for which it locally owns most of the required tetrahedra. The other MPI ranks send their local tetrahedra overlapping this leaf node to R and R starts depositing the elements as discussed in detail in Section 6, while, in parallel, work is assigned to other MPI ranks. Instead of first constructing the tetrahedra of the Lagrangian blocks and then sending them to the target rank, each compute node sends complete 8^3 subblocks of particles and R constructs the tessellation elements locally, thereby drastically reducing the amount of transferred data.

(B) *Sending Oct-tree Nodes:.* Each MPI rank enters a loop, picks the next leaf node for which it owns local tetrahedra and deposits their mass, as discussed in Section 6. Concurrently, the ranks reduce a bit mask that indicates which of the leaf nodes are locally finished. Once a certain leaf node has been globally processed, all ranks that contributed mass, globally reduce the associated array of masses. In case the deposit process is finished locally but not globally, the result is buffered in a list, in order to avoid that the rank is idling. However, once the buffer’s maximal storage is reached, the rank has to wait until at least one of its buffered leaf nodes is globally finished.

6. Mass Deposit

As discussed in the last Section, concurrent computation and communication is enabled by launching several threads per compute node: one communication thread for exchanging data between compute nodes, as well as at least one worker thread managing the deposition of the tetrahedra masses. Here we will give an overview of the multi-threaded mass deposit approach and defer the CPU and GPU specific implementation details to the next Subsections.

In both cases, the worker threads keep running until all oct-tree leaf nodes have been processed. The Lagrangian cell blocks, that overlap the spatial extent of the current leaf node, are distributed to the available worker threads. We found that splitting them into 10 times more groups, than the number of worker threads, leads to good results in terms of dynamic load balancing between the

worker threads. Each thread allocates its own private memory buffer to accumulate the mass contributions. The mass deposit step involves the computation of the exact intersection volumes between the tetrahedra and the cubical grid cells and will be discussed in detail in the Subsection 6.3. Once a worker thread has deposited all mass associated with its tetrahedra, it is assigned the next set of Lagrangian cell blocks and once all blocks have been processed, their private mass buffers are added and the communication thread is signaled that the worker threads are ready for new work.

6.1. CPU Implementation

In the CPU case, each worker thread operates on one cell L of its assigned Lagrangian grid blocks at a time. The 8 vertices of L are gathered, their minimal axis-aligned bounding box is constructed and tested for intersection with the extent of the leaf node’s deposit grid patch. In the case of no intersection, L ’s 6 tetrahedra are skipped and the next cell is processed. Otherwise the first of the 6 tetrahedra, T_0 , is constructed, its minimal bounding box is determined and the worker thread loops over all cells C_i of the deposit grid patch that overlap the bounding box of T_0 . For each cell C_i , we first test for trivial intersection configurations between C_i and T_0 , i. e. no intersection, C_i completely inside T_0 or vice versa, which is implemented by computing the relative orientation of the vertices of T_0 with respect to the axis-aligned faces of C_i . Otherwise, the more expensive algorithm discussed in Subsection 6.3 is used to compute the exact intersection volume. The resulting volume is transformed to its mass equivalent and stored in the thread’s private memory location for cell C_i and the next tetrahedron of L is processed.

6.2. GPU Implementation

In the GPU case, we start one CPU thread for each available local GPU and keep it running, until all leaf nodes of the grid structure have been processed. Each CPU thread allocates private GPU memory to store the Lagrangian grid block as well as a buffer to accumulate the mass contributions.

On the GPU, code divergence can severely affect overall performance, since sets of threads operate in lock-step and divergence by different code paths causes subsets of the GPU threads to idle, resulting in an underutilization of the available hardware resources. This poses a challenge for the geometry intersection, since the amount of work for the tetrahedra differs substantially, depending, for example, on the number of deposit cells they cover and on how many non-trivial intersection configurations there are with respect to the covered cells.

On current *NVIDIA* GPU architectures, sets of 32 threads, called *lanes*, form a *warp* and operate in lock-step. Hence, assigning one tetrahedron to each *lane*, as done for example in the 2D triangle rasterization approach *FreePipe* [22], can result in only one of 32 threads performing useful work. One potential solution is to launch different *GPU kernels* to first classify the cells for each tetrahedron and buffer the results in global GPU memory, next operate on the inexpensive trivial intersection configurations and finally process the expensive non-trivial

ones, similar to the techniques discussed for 2D triangle rasterization in *CUDA raster* [23]. However, in the 3-dimensional case, this approach quickly exceeds the available global GPU memory due to the drastically larger number of cells in the 3D deposit grids, as compared to the 2-dimensional framebuffer.

We therefore follow a different approach, that avoids the usage of additional global memory by letting a whole *warp* operate on one tetrahedron at a time, using a single GPU kernel. Each warp picks its own Lagrangian cell, samples its vertices, tests their bounding box for intersection with the octree node and, in case of an intersection, constructs the first of the 6 tetrahedra for the cell. As shown in Figure 3, each *lane* of the *warp* picks a different cell in the deposit grid patch and classifies the intersection configuration in lock-step. Since the trivial cases are not computationally expensive and cause only minimal thread divergence, they are processed immediately. Each lane uses an atomic counter to update the GPU’s global memory block for the mass contribution. However, in case a *lane* detects a non-trivial configuration, it does not call the more expensive intersection routine discussed in Subsection 6.3 immediately, but rather stores the cell’s ID in the fast, low-latency *shared memory*. We use a buffer size of 64 single precision integers, that are shared between the *lanes*, and updated using an atomic counter in *shared memory*. The lanes continue to classify cells, until the number of IDs, stored in the *shared memory* buffer, exceed 31. In this case, each *lanes* picks one buffered ID and calls the exact intersection routine for its cell. Once all lanes in the warp returned from the call, they classify the next set of 32 cells in lock-step. For our test cases, this approach reduced thread divergence substantially and lead to performance increases of about 20x compared to an alternative “one-tetrahedron per lane” approach.

6.3. Tetrahedron-Cube Intersection

In this Subsection, we describe our algorithm for computing the volume of the intersection between a tetrahedron T and a cubical cell C . For the sake of simplicity, we explain the algorithm in 2D, since the generalization to 3D is straightforward. So the task is to compute the area of the intersection between a triangle T and the quadratic cell C . Let us assume that the cell’s lower left corner is at $(x = 0, y = 0)$ and its upper right at $(x = 1, y = 1)$, as depicted in Figure 4 (a).

The first step is to intersect T with the line defined by $(x = 0, y)$. If the entire triangle is located on the half-plane defined by $(x \leq 0, y)$, the intersection volume is zero and the algorithm terminates. Otherwise the resulting polygon, located on the half-plane $(x > 0, y)$ that includes C , is triangulated by up to two triangles, as shown in Figure 4 (b). Next, the newly generated triangles are tested for intersection with the line $(x = 1, y)$, the resulting interior region is again triangulated and the procedure is repeated for the lines $(x, y = 0)$ and $(x, y = 1)$, and the intersection area is given by the sum of the areas of the resulting triangles. The approach operates analogously in 3-dimensions, where the tetrahedron is iteratively split against the 2D planes defined by the faces of the cell. In order to speed up the triangulation of auxiliary polygons, we precompute all different cases and store them in a *look-up table*. The location

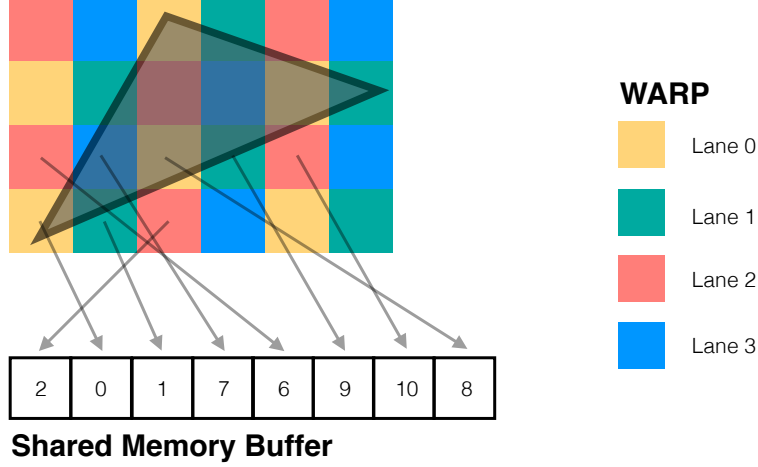


Figure 3: 2D example of the GPU rasterization approach for a warp size of 4. The lanes in the warp, depicted by different colors, classify 4 cells in lock-step. Using an atomic counter, the IDs of cells intersecting the boundary of the triangle, are stored in a buffer in the fast shared memory.

of the vertices of T relative to P defines a bitmask that serves as a lookup index into the table, which returns the number of resulting tetrahedra as well as the connectivity information to construct the intermediate geometry. Instead of carrying out the algorithm as sketched above for all three dimensions, for the third dimension, we triangulate the parts of the polygons outside C 's halfspace, instead the one inside, and subtract its volume from the one of the interior tetrahedra, since this generally reduces the amount of generated geometry.

A possible GPU implementation is to cache the intermediate tetrahedra and reuse them for each new dimension that is processed. However, on the GPU, the fast *shared memory* is too small to store all geometry, so it would have to be moved to slower global memory, thereby degrading overall performance.

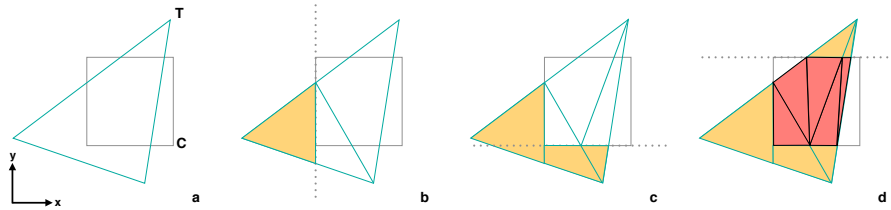


Figure 4: Computing the area of the intersection between cell C and triangle T , by iteratively splitting T against lines defined by the edges of C followed by a triangulation of the resulting polygon on the half-space that includes C .

Therefore, we avoid to cache intermediate tetrahedra and prune each tetrahedron separately against all cell’s faces, before the next intermediate tetrahedron is processed. Although this involves redundant computations, it turns out to increase performance on massively parallel graphics hardware, where computation is less expensive than data movement. However, also on the CPU, the latter led to a performance increase.

7. Results and Discussions

We conducted our experiments on the *Sherlock* and *XStream* HPC clusters at the Stanford Research Computing Center (SRCC). *Sherlock*’s hardware resources include 120 general compute nodes, each with a dual socket *Intel Xeon CPU E5-2650 v2* at 2.60 GHz, 8 cores per socket and 64 GB DDR3 RAM. *XStream* consists of 65 compute nodes, each equipped with 2 x *Intel Xeon CPU E5-2680 v2 @ 2.80GHz* (10 cores per socket), 256 GB of RAM and 8 x *NVIDIA Tesla K80* (16 logical GPUs). Both clusters are interconnected with FDR Infiniband and have access to a PB sized Lustre parallel file system. For our tests we used simulations with 4096^3 and 2048^3 particles from the *Dark Sky Simulations: Early Data Release* [24].

7.1. Strong Scaling

The strong scaling tests utilized between 128 and 2048 CPU cores on *Sherlock*, with one MPI rank per compute node and 8 threads per MPI rank. The test problem was the exact mass deposit of a 2048^3 particles N-body simulation onto a fully refined octree with 4 levels of refinement and 128^3 cells per node, resulting in a total grid resolution of 2048^3 cells. Tables 5 and 6 as well as Figure 7 summarize the results for the two different communication strategies discussed in Section 5 - exchanging point data (A) versus exchanging deposit grid arrays between compute nodes (B). For approach (B), up to 5000 leaf nodes per compute node were cached locally, before reducing the result across the cluster. As shown in tables 5 and 6, the performance of approach (A) was between 15% to 45% faster than (B)’s. Also in terms of achieved speed-ups approach (A), which shows almost perfect scaling up to 1024 cores, outperformed (B). For 2048 cores, the speed-up was reduced from 16 to about 11, due to increased overhead of communication between the cluster nodes.

7.2. Weak Scaling

In order to ensure that the complexity of the workload for the different datasets used for the weak scaling test scales linearly with the number of utilized cores, the different datasets were generated analytically, by placing the dark matter particles onto a uniform grid and adding randomized positive or negative offsets of up to one cell width in each direction to the particle positions. The number of particles and the number of cells in the deposit grid was successively increased by a factor of two, ranging from 512^3 to 2048^3 particles, with 256^3 to 1024^3 cells in the deposit grid structure. The datasets were processed utilizing

# CPU cores	Time (min)	Speedup
128	603	1.0
256	331	1.8
512	143	4.2
1024	81	7.4
2048	53	11.2

Figure 5: Strong scaling results for communication strategy (A) for depositing the mass associated with a 2048^3 particles N-body simulation onto a fully refined octree with 4 levels of refinement and 128^3 cells per node, resulting in a total grid resolution of 2048^3 cells.

# cores	Time (min)	Speedup
128	712	1.0
256	458	1.6
512	266	2.7
1024	129	5.0
2048	77	9.2

Figure 6: Strong scaling results for communication alternative (B), using the same test problem as in Table 5.

between 32 and 2048 cores on 1 up to 64 nodes on the Sherlock cluster, doubling the number of nodes between consecutive tasks. The resulting wall clock times for communication strategy (A) are given in Figure 8.

7.3. GPU Performance

The performance between the CPU and GPU version of the code discussed in Section 6, was conducted on one node of the *XStream* GPU cluster. The CPU version utilized 40 threads on the dual Intel Xeon CPU E5-2650 v2 (2x10 cores with hyperthreading), whereas the GPU version was run on one *Nvidia K80*. The test problem was the mass deposit for a N-body simulation with 2048^3 particles onto a fully refined octree with 4 levels of refinement and 128^3 cells per node, resulting in a total grid resolution of 2048^3 cells. The CPU version took about 1995 minutes to complete, whereas the GPU version was finished in about 230 minutes, so the achieved GPU speedup was about 8.7. Figure 9 shows the result of a strong scaling test on a single node of the *Xstream* cluster, utilized between 1 and all 16 available GPUs. The test dataset was a 1024^3 particle dataset. The speedup increased roughly linearly with the number of GPUs with a slope of about 0.63, due to the increased overhead of transferring the point data from the CPU to several GPUs and reducing the local deposit grid arrays back on the CPU.

We further performed an adaptive mass deposit test using a 4096^3 particle N-body dataset, using a leaf node size of 64^3 cells per node and a maximum of 6 refinement levels, resulting in an effective resolution of 8192^3 cells on the

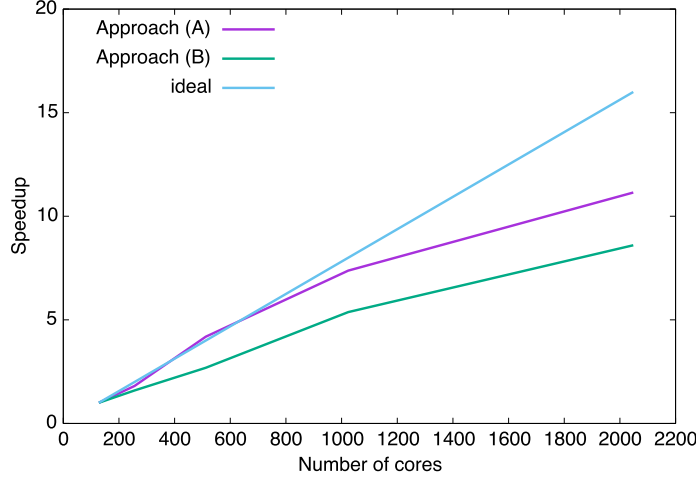


Figure 7: Strong scaling results for 2048^3 particles.

highest level of resolution. The test was run on 16 compute nodes of *XStream*, utilized all available 8 *Nvidia K80* cards per node and finished in 46 minutes. Figure 10 shows a visualization of the multi-resolution density field with direct volume rendering.

8. Summary and Future Work

We presented an approach for the distributed computation of accurate density fields from large N-body dark matter simulations using the phase-space element technique, that is tailored to massively parallel cluster architectures equipped with accelerators. We employed an adaptive grid structure to sample the densities onto cubical cells, adapting the resolution according to the features of the underlying tessellation. We proposed an efficient GPU implementation for the computationally expensive operation of intersecting the tetrahedral tessellation elements with the cubical cells of the leaf nodes of the deposit grid hierarchy, that achieved a speedup of almost an order of magnitude compared to a CPU version. We further presented a flexible dynamic load balancing strategy and demonstrated the overall good weak and strong scaling performance of our approach with several datasets. Our experiments showed, that it is beneficial to communicate particle data instead reducing deposit grid patches in terms of overall performance and scaling features.

We see various directions for future work. It would be interesting to compare the performance of the GPU implementation with that executed on the massively parallel *Intel Xeon Phi* coprocessors. We would also like to investigate if the proposed solution can be extended and applied to *in-situ* scenarios, i.e., performed alongside the underlying simulation, by sharing the available hard-

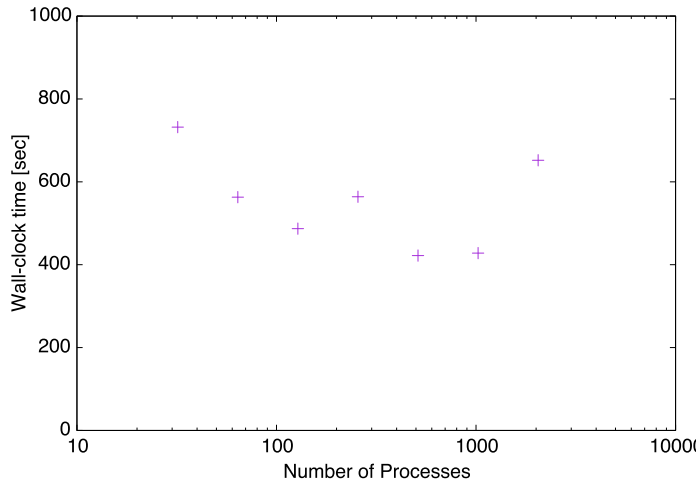


Figure 8: Weak scaling results for a mass deposit problem using 512^3 to 2048^3 particles running on between 32 and 2048 processes.

ware resources. It would also be interesting to test alternative data structures to organize the adaptive deposit grid, for example *kD-trees* or *block-structured AMR* hierarchies. Furthermore, in addition to the mass deposit onto the leafs nodes of the oct-tree structure, generating coarser representations for the internal nodes would be beneficial for interactive visualization approaches, like direct volume rendering, that employ multi-resolution representations of the data to achieve interactive frame rates.

Our implementation is available at <https://github.com/kaehlerr/ADECO>.

9. Acknowledgments

We are very grateful to Tom Abel and Devon Powell for useful discussions on this topic. We would also like to thank the *Dark Sky Simulations* collaboration for making the data available, in particular Sam Skillman for his advice regarding the data format. This work used the XStream computational resource, supported by the National Science Foundation Major Research Instrumentation program (ACI-1429830). Parts of the computing for this project was performed on the Sherlock cluster. We would like to thank Stanford University and the Stanford Research Computing Center for providing computational resources and support that have contributed to these research results. We would also like to thank Nvidia for supporting KIPAC’s computing center with several GPUs.

References

- [1] A. V. Kravtsov, A. A. Klypin, A. M. Khokhlov, Adaptive refinement tree: A new high-resolution n-body code for cosmological simulations, *The As-*

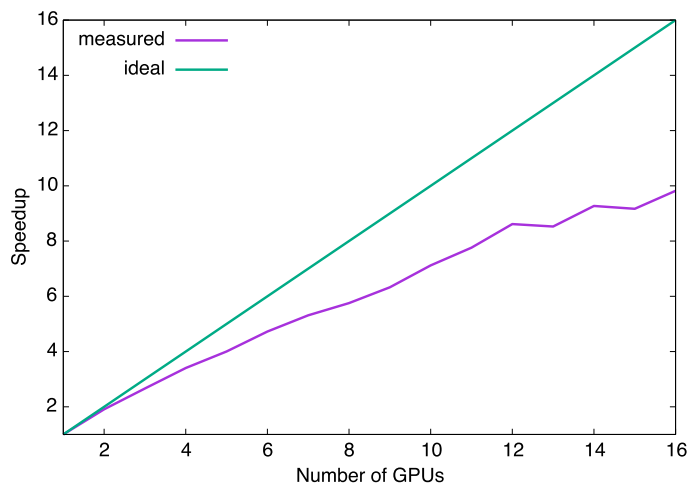


Figure 9: Ideal and measured GPU strong scaling results for 1024^3 particles and 1 to 16 GPUs on a single node of the Xstream cluster.

trophysical Journal Supplement Series 111 (1) (1997) 73.

URL <http://stacks.iop.org/0067-0049/111/i=1/a=73>

- [2] R. Teyssier, Cosmological hydrodynamics with adaptive mesh refinement: a new high resolution code called ramses, *Astron. Astrophys.* 385 (2002) 337–364. [arXiv:astro-ph/0111367](#), doi:10.1051/0004-6361:20011817.
- [3] V. Springel, The Cosmological Simulation Code Gadget-2, *Monthly Notices of the Royal Astronomical Society* 364.
- [4] S. Habib, V. Morozov, N. Frontiere, H. Finkel, A. Pope, K. Heitmann, Hacc: Extreme scaling and performance across diverse architectures, in: *Proceedings of the International Conference on High Performance Computing, Networking, Storage and Analysis, SC '13*, ACM, New York, NY, USA, 2013, pp. 6:1–6:10. doi:10.1145/2503210.2504566. URL <http://doi.acm.org/10.1145/2503210.2504566>
- [5] M. S. Warren, 2hot: An improved parallel hashed oct-tree n-body algorithm for cosmological simulation, in: *Proceedings of the International Conference on High Performance Computing, Networking, Storage and Analysis, SC '13*, ACM, New York, NY, USA, 2013, pp. 72:1–72:12. doi:10.1145/2503210.2503220. URL <http://doi.acm.org/10.1145/2503210.2503220>
- [6] G. L. Bryan, M. L. Norman, B. W. O’Shea, T. Abel, J. H. Wise, M. J. Turk, D. R. Reynolds, D. C. Collins, P. Wang, S. W. Skillman, B. Smith, R. P. Harkness, J. Bordner, J.-h. Kim, M. Kuhlen, H. Xu, N. Goldbaum, C. Hummels, A. G. Kritsuk, E. Tasker, S. Skory, C. M. Simpson, O. Hahn,

- J. S. Oishi, G. C. So, F. Zhao, R. Cen, Y. Li, Enzo Collaboration, ENZO: An Adaptive Mesh Refinement Code for Astrophysics, *apjs* 211 (2014) 19. [arXiv:1307.2265](#), [doi:10.1088/0067-0049/211/2/19](#).
- [7] A. S. Almgren, J. B. Bell, M. J. Lijewski, Z. Luki, E. V. Andel, Nyx: A massively parallel amr code for computational cosmology, *The Astrophysical Journal* 765 (1) (2013) 39.
URL <http://stacks.iop.org/0004-637X/765/i=1/a=39>
- [8] R. W. Hockney, J. W. Eastwood, *Computer Simulation Using Particles*, Taylor & Francis, Inc., Bristol, PA, USA, 1988.
- [9] C. K. Birdsall, D. Fuss, Clouds-in-clouds, clouds-in-cells physics for many-body plasma simulation, *Journal of Computational Physics* 3 (1969) 494–511. [doi:10.1016/0021-9991\(69\)90058-8](#).
- [10] J. J. Monaghan, An introduction to SPH, *Computer Physics Communications* 48 (1988) 89–96. [doi:10.1016/0010-4655\(88\)90026-4](#).
- [11] M. C. Neyrinck, ZOBOV: a parameter-free void-finding algorithm, *mnras* 386 (2008) 2101–2109. [arXiv:0712.3049](#), [doi:10.1111/j.1365-2966.2008.13180.x](#).
- [12] S. Shandarin, S. Habib, K. Heitmann, Cosmic web, multistream flows, and tessellations, *Phys. Rev. D* 85 (2012) 083005. [doi:10.1103/PhysRevD.85.083005](#).
URL <http://link.aps.org/doi/10.1103/PhysRevD.85.083005>
- [13] T. Abel, O. Hahn, R. Kaehler, Tracing the dark matter sheet in phase space, *Monthly Notices of the Royal Astronomical Society* 427 (1) (2012) 61–76. [arXiv:http://mnras.oxfordjournals.org/content/427/1/61.full.pdf+html](#), [doi:10.1111/j.1365-2966.2012.21754.x](#).
URL <http://mnras.oxfordjournals.org/content/427/1/61.abstract>
- [14] O. Hahn, T. Abel, R. Kaehler, A new approach to simulating collisionless dark matter fluids, *Mon. Not. Roy. Astron. Soc.* 434 (2013) 1171. [arXiv:1210.6652](#), [doi:10.1093/mnras/stt1061](#).
- [15] R. Kaehler, O. Hahn, T. Abel, A novel approach to visualizing dark matter simulations, *IEEE Transactions on Visualization and Computer Graphics* 18 (12) (2012) 2078–2087. [doi:doi.ieeecomputersociety.org/10.1109/TVCG.2012.187](#).
- [16] O. Igouchine, N. Leaf, K.-L. Ma, Volume rendering dark matter simulations using cell projection and order-independent transparency, in: *SIGGRAPH ASIA 2016 Symposium on Visualization, SA '16*, ACM, New York, NY, USA, 2016, pp. 8:1–8:8. [doi:10.1145/3002151.3002163](#).
URL <http://doi.acm.org/10.1145/3002151.3002163>

- [17] R. E. Angulo, R. Chen, S. Hilbert, T. Abel, Towards noiseless gravitational lensing simulations, *Mon. Not. Roy. Astron. Soc.* 444 (3) (2014) 2925–2937. [arXiv:1309.1161](#), [doi:10.1093/mnras/stu1608](#).
- [18] O. Hahn, R. E. Angulo, T. Abel, The Properties of Cosmic Velocity Fields, *Mon. Not. Roy. Astron. Soc.* 454 (4) (2015) 3920–3937. [arXiv:1404.2280](#), [doi:10.1093/mnras/stv2179](#).
- [19] O. Hahn, R. E. Angulo, An adaptively refined phase space element method for cosmological simulations and collisionless dynamics, *Mon. Not. Roy. Astron. Soc.* 455 (1) (2016) 1115–1133. [arXiv:1501.01959](#), [doi:10.1093/mnras/stv2304](#).
- [20] D. Powell, T. Abel, An exact general remeshing scheme applied to physically conservative voxelization, *J. Comput. Phys.* 297 (2015) 340–356. [arXiv:1412.4941](#), [doi:10.1016/j.jcp.2015.05.022](#).
- [21] P. J. E. Peebles, *Principles of Physical Cosmology*, 1993.
- [22] F. Liu, M.-C. Huang, X.-H. Liu, E.-H. Wu, Freepipe: A programmable parallel rendering architecture for efficient multi-fragment effects, in: *Proceedings of the 2010 ACM SIGGRAPH Symposium on Interactive 3D Graphics and Games, I3D '10*, ACM, New York, NY, USA, 2010, pp. 75–82. [doi:10.1145/1730804.1730817](#).
URL <http://doi.acm.org/10.1145/1730804.1730817>
- [23] S. Laine, T. Karras, High-performance software rasterization on gpus, in: *Proceedings of the ACM SIGGRAPH Symposium on High Performance Graphics, HPG '11*, ACM, New York, NY, USA, 2011, pp. 79–88. [doi:10.1145/2018323.2018337](#).
URL <http://doi.acm.org/10.1145/2018323.2018337>
- [24] S. W. Skillman, M. S. Warren, M. J. Turk, R. H. Wechsler, D. E. Holz, P. M. Sutter, Dark Sky Simulations: Early Data Release [arXiv:1407.2600](#).

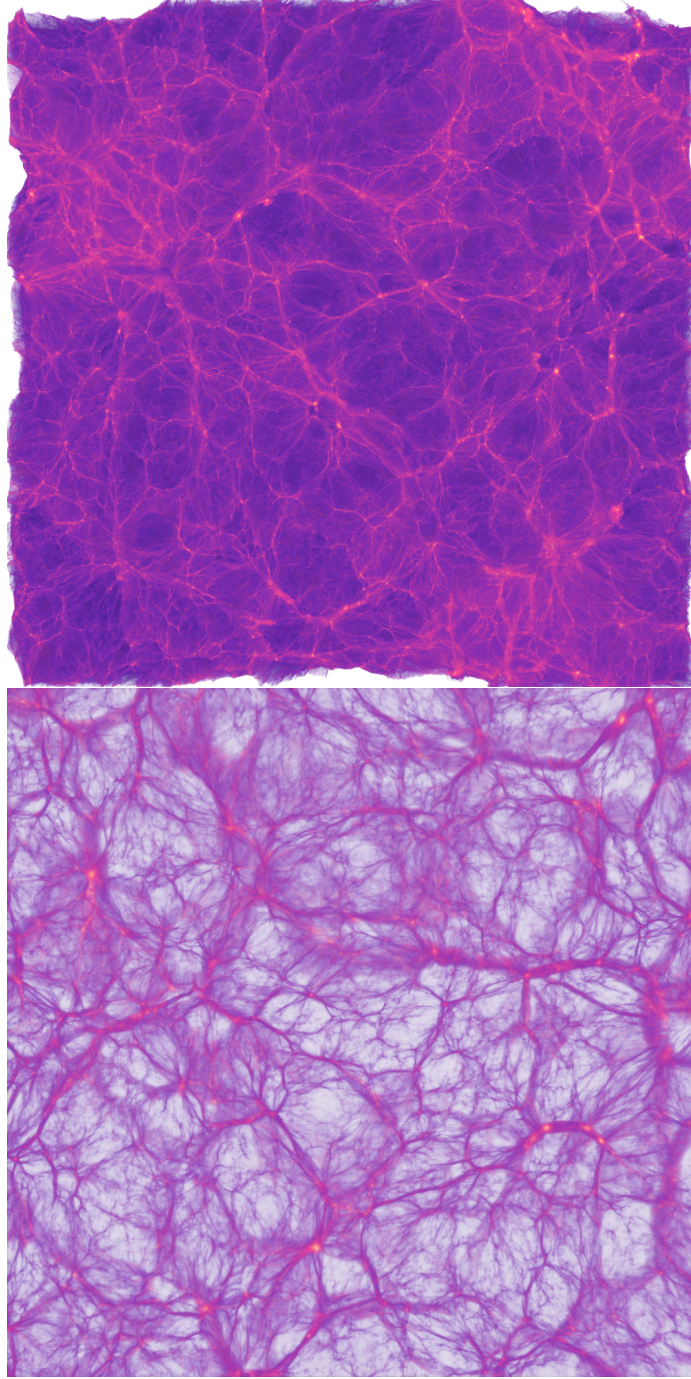


Figure 10: Direct volume rendering of an N-body simulation with 4096^3 particles. The mass was resampled onto an oct-tree data structure with an effective resolution of 8192^3 cells. The upper part shows the whole domain, whereas the lower one depicts a zoomed view of a thin slice through the volume.